Structural, optical, XPS and magnetic properties of Zn particles capped by ZnO nanoparticles

Iu.G. Morozov, O.V. Belousova, D. Ortega, M.-K. Mafina, M.V. Kuznetcov

PII: S0925-8388(15)00383-7
DOI: http://dx.doi.org/10.1016/j.jallcom.2015.01.285
Reference: JALCOM 33349

To appear in: *Journal of Alloys and Compounds*

Received Date: 22 November 2014
Revised Date: 15 January 2015
Accepted Date: 31 January 2015

Please cite this article as: Iu.G. Morozov, O.V. Belousova, D. Ortega, M.-K. Mafina, M.V. Kuznetcov, Structural, optical, XPS and magnetic properties of Zn particles capped by ZnO nanoparticles, *Journal of Alloys and Compounds* (2015), doi: http://dx.doi.org/10.1016/j.jallcom.2015.01.285

Structural, optical, XPS and magnetic properties of Zn particles capped by ZnO nanoparticles

Iu.G. Morozov[a,*], O.V. Belousova[a], D. Ortega[b], M.-K. Mafina[c], M.V. Kuznetcov[d]

[a]*Institute of Structural Macrokinetics and Materials Science, Russian Academy of Sciences, Academician Osipyan Street 8, Chernogolovka, Moscow Region, 142432 Russia*
[b]*Instituto Madrileño de Estudios Avanzados en Nanociencia (IMDEA-Nanociencia), Cantoblanco 28049, Madrid, Spain*
[c]*School of Engineering and Materials Science, Queen Mary University of London, Mile End, Eng, 231, London E1 4NS, UK*
[d]*Department of Chemistry, Materials Chemistry Research Centre, University College London, 20 Gordon Street, London WC1H 0AJ, UK*

A B S T R A C T

Spherical zinc particles ranging from 42 to 760 nm in average size and capped with plate-like zinc oxide particles of 10-30 nm in sizes have been prepared by levitation-jet aerosol synthesis through condensation of zinc vapor in an inert/oxidizer gas flow. The nanoparticles have been characterized by transmission electron microscopy (TEM), X-ray diffraction (XRD), BET measurements, ultra violet visible (UV-Vis) spectroscopy, Fourier transform infrared (FT-IR) spectroscopy, Raman spectroscopy, X-ray electron spectroscopy (XPS), superconducting quantum interference device (SQUID), and vibrating-sample magnetometer (VSM). Magnetic and XRD data indicate that the observed ferromagnetic ordering related to the changes in unit-cell volume of Zn in the Zn/ZnO interface of the nanoparticles. These results are in good correlation with the optical measurements data.

Keywords:
Nanoparticles (NPs)
Levitation-jet generator
Zinc oxide (ZnO)
Optical properties
Room temperature ferromagnetism (RTFM)

1. Introduction

ZnO has attracted increasingly worldwide attention in the past few decades due to its unique properties and a large number of potential applications such as transparent conductive contacts [1], dye-sensitized photoelectrochemical solar cells [2], ZnO/Cu_2O solar cell heterojunctions [3-5], laser diodes [6], ultraviolet lasers [7], thin film transistors [8], gas sensors [9], optoelectronic and piezoelectric applications to surface acoustic wave devices [10], and so on. Zinc oxide (ZnO) is a material usually characterized by its wide band gap of 3.37 eV at room temperature. This band gap can be excited by using short wavelength emissions such as UV radiation; high excitonic binding energy, around 60 meV; very short luminescence life time; to allow changes in the material's properties to

* Corresponding author. *Tel.: +7 49652 46368.*
E-mail addresses: yugmor@hotmail.com (Iu.G. Morozov), daniel.ortega@imdea.org (D. Ortega), m.k.mafina@qmul.ac.uk (M.-K. Mafina), maxim1968@mail.ru (M.V. Kuznetcov)

improve mechanical properties, as well as produce a reasonably cheap and environment friendly material [11, 12].

In the last decade some of the nonmagnetic metals oxides have been widely investigated because of their ferromagnetic behavior at room temperature (RTFM) in nanosized form which is very important for the spin electronics applications [13]. RTFM was discovered in the doped ZnO [14] as well as in the undoped material too [15]. The existance of RFTM in the undoped ZnO stimulated discussion about the role of intrinsic defects in this phenomenon. For the Zn–O system, also known as a pristine oxide, it was shown that defects, such as Zn and O vacancies [16-21], Zn interstitials [22], grain boundaries [23] and lattice distortions [24], might contribute to the development of RTFM. If all these defects are indeed responsible for the ferromagnetism in thin films and nanoparticles, they should be thermodynamically stable at least to room temperature, and magnetic exchange interaction between them should be strong enough for the existence of ferromagnetism to be feasible [25]. However, there remain a number of unanswered questions regarding the magnetic properties of such material [25]. Exactly which defect species or group of defects are responsible for the development of magnetic moments? How is long-range exchange interaction between local moments brought about in the pristine oxide? How does the total magnetization of a material depend on defect density and how can its magnetization value be optimized? Unfortunately, first principles theoretical calculations in this area of research have not yet provided unique answers to these questions [26].

Since a low dimensionality of samples is critical to the ability to observe RTFM, studies of nanoparticles (which have the largest specific surface area) have a number of advantages over those of films REF. The main advantage of using nanoparticles is the ease in determining more accurate specific magnetization data of the materials, which is necessary for the ability to adequately compare between samples prepared under different techniques and conditions [27]. We have obtained zinc nanoparticles of various sizes, containing a different amount of an oxide component, which allowed us to model a situation analogous to that occurring in thin oxidized Zn films and investigate the basic physicochemical properties and specific magnetization of the resultant material [28]. It is well known that optical properties of ZnO nanoparticles are strongly dependent on changes in the synthesis conditions [29, 30], defects [31-33], microstructure, crystallite sizes, morphology [34-37], and others, therefore, we used the levitation-jet generator [38], which offers an easier manufacturing process of nanoparticles with an appropriate surface area for study of its optical properties. In the present paper, we are focusing our attention on the interrelation between the development of RTFM, the structural and optical properties of Zn/ZnO nanoparticles (NPs), exhibiting RTFM, which had not been

establish earlier [39, 40].

2. Experimental

Zn/ZnO aerosol nanoparticles were obtained by using modified Gen levitation-jet generator described in detail according to Morozov *et.al.* [41]. In this technique, a pure zinc wire at 99.9 % with a diameter of 3 mm was placed in a quartz tube with an inner diameter of 14 mm. The end of the wire was heated up by the electromagnetic field generated using a counter-current inductor (encasing the tube) until the metal began to vaporize directly from the solid phase at a temperature lower than the boiling point of zinc. This inductor powered by an industrial high frequency generator (0.44 MHz). The vaporizing wire was blown down by an adjustable stream of gas (He or Ar) and moved into the inductor at a constant preset speed as the metal vaporized and the cross-sectional size of the wire diminished. In some experiments, special actions were taken for an additional NPs oxidization in the way of gaseous oxygen or air adding in the combined mode [28]. The formation of aerosol nanoparticles takes place in a region around the evaporated metal wire end where Zn atoms condense and eventually form primer clusters [42]. ZnO content depends on the gas-phase oxidation rate of the particles in comparison with the metal clusters coalescence rate during condensation and post-condensation processes. This competition may be the one of the main reason in the appearance of real morphology in Zn/ZnO NPs. Once the above process was completed, the resultant grey powder was collected on a cloth filter and hereinafter removed from the filter into a particle container. Special measures have been taken in order to prevent any influence of alien magnetic contaminants for the NPs properties [43].

The NPs crystal structure was studied by X-ray powder diffractometer ADP-2 (Cu K_α radiation). Their phase composition was determined using JCPDS PDF database (release 2011) and Crystallographica SearchMatch ver. 3.102 software. Rietveld analysis (PowderCell 2.0) of X-ray diffraction patterns was used to evaluate the ratio of crystalline phases in NPs. Its morphology and dimensions were examined using transmission electron microscope JEOL JEM-1200EX2. Specific surface area of NPS was determined by 4-point nitrogen physical sorption BET measurements using META SORBI-M device. Examination of the NPs optical properties were carried out by means of various techniques; (1) UV-vis spectra of NPs were recorded on a by Lambda950 (Perkin Elmer) using the integrated sphere detector. (2) Fourier transform infrared (FT-IR) spectra were recorded in solid phase using Tensor 27 spectrometer with the attenuated total reflectance (ATR) accessory (Bruker) in the frequency range of 400–4000 cm^{-1}. (3) Raman spectra were recorded at room temperature using InVia Raman Renishaw and

confocal microscope Leica DMLM apparatus with an air-cooled, charge coupled device and coupled with He-Cd and Ar lasers emitting at 325 nm and 514 nm, respectively. XPS data was recorded using a Thermo Scientific X-ray Photoelectron Spectrometer. It utilizes a monochromated Al K_α (1486.6 eV) source running at a power of 72 W with a pass energy of 50 eV was used for high resolution region scans and 200 eV for survey scans; finally, for charge correction a 1 point scale with the C1s peak shifted to 285.0 eV was used.

Magnetic properties of NPs were measured by means of Quantum Design hybrid VSM-SQUID magnetometer, which was calibrated using a standard Dy_2O_3 sample with a relative accuracy of 1 x 10^{-6} emu, at room temperature [44]. During the experiments, the magnetic field was ramped from zero to 70 kOe at 300 K. Sample mass (a few mg) was determined with relative accuracy of ±2 x 10^{-4} mg. We have subtracted the rather low magnetic moment of the samples from the experimental outputs of the diamagnetic contribution associated with appropriate sample container. It should be also noted that applied magnetic field (H) values were precisely corrected by comparing the experimental fields with those expected for the Dy_2O_3. A part of NPs samples was characterized in applied magnetic fields of up to 13 kOe using EG&G PARC M4500 vibrating sample magnetometer.

3. Results and discussion

3.1 Zn/ZnO NPs morphology and BET characterization

Figs. 1a-1f show TEM micrographs of NPs. Most of the particles are seen to be rather large (about hundreds nm in sizes) and common spherical in shape. In these figures, irregular shaped plate-like nanoparticles (10 - 30 nm in sizes) well seen on the surface of the large particles. These particles are very morphologically similar to the capped ferromagnetic ZnO nanoparticles (10-30 nm in sizes) previously observed as a result of syntheses with the different kinds of precursors [45-48]. As the process for large particles, preparation takes place under very low amount of air (a technological feature) we may suggest that the particles shape is a result of the Zn clusters aggregation followed by an inert gas cooling. Plate-like nanoparticles most likely are some fragments of Zn aggregates, which managed full oxidation and then being hot cleave on the cold surface of the large particles. In the case of small NPs (fig. 1c), the synthesis process takes place under essential oxidizer content in the net gas flow (Table 1). That time-limited the condensation zone [38, 41] and in result Zn and ZnO as it may see in the fig. 1c probably form the separate nanoparticles, with the latter became a tetrapod-shaped [49] and the above-mentioned Zn/ZnO capped morphology be non-obvious.

Table 1 lists the specific surface areas (S) of the various NPs studied, from which their average size d_{BET} (nm) evaluated. It approached to the morphological estimated average size of

the large nanoparticles projections in all of the micrographs obtained.

Table 1

Main properties of Zn/ZnO NPs synthesized by using modified Gen levitation-jet generator. d_{BET} - average particle size obtained from BET measurements; V_{xrd} - ZnO content; E_g - the energy gap; V - unit-cell volume; σ_{max} - maximum specific magnetization; S - specific surface area.

Sample ID	Synthesis conditions	d_{BET} (nm)	V_{xrd} (at. %) ZnO	E_g (eV)	$V \times 10^4$ (nm^3) Zn	σ_{max} (emu/g)	S (m^2/g)
Z1	Ar – 83 l/h, Zn – 60 g/h	650	1.8		349.68	0.103	1.29 ± 0.06
Z2	He – 500 l/h, air – 60 l/h, Zn – 60 g/h	57	53.9	3.27	350.12	0.007	16.9 ± 0.24
Z3	He – 500 l/h, Zn – 60 g/h	275	5.3		349.60	0.031	3.11 ± 0.13
Z4	He – 250 l/h, Zn – 60 g/h	590	10.0		349.68	0.250	1.46 ± 0.09
Z5	He – 1200 l/h, Zn – 60 g/h	135	14.0	3.10	350.59	0.003	6.22 ± 0.11
Z6	He – 500 l/h, O_2 – 60 l/h, Zn – 60 g/h	42	54.9	3.30	349.51	0.013	22.7 ± 2.02
Z7	He – 500 l/h, air – 110 l/h, Zn – 50 g/h	43	64.2	3.30	349.95	0.035	22.6 ± 2.34
Z8	Ar – 40 l/h, Zn – 60 g/h	610	2.0	3.23	350.04	0.005	1.38 ± 0.11
Z10	Ar – 300 l/h, Zn – 60 g/h	410	0	3.19	346.73	0.003	2.05 ± 0.12
Z11	He – 115 l/h, Zn – 80 g/h	550	0		350.19	0.020	1.60 ± 0.11
Z12	He – 400 l/h, Zn – 60 g/h	430	3.8	3.14	349.87	0.001	1.98 ± 0.18
Z14	He – 200 l/h, Zn – 60 g/h	300	3.5	3.14	349.74	0.029	2.81 ± 0.04
Z15	Ar – 83 l/h, Zn – 60 g/h	760	~0		348.68	0.010	1.11 ± 0.04
Z16	He – 290 l/h, Zn – 60 g/h	450	4.8		351.45	0.022	1.95 ± 0.91
Z17	He – 250 l/h, Zn – 30 g/h	290	5.7		349.7	0.270	3.08 ± 0.12

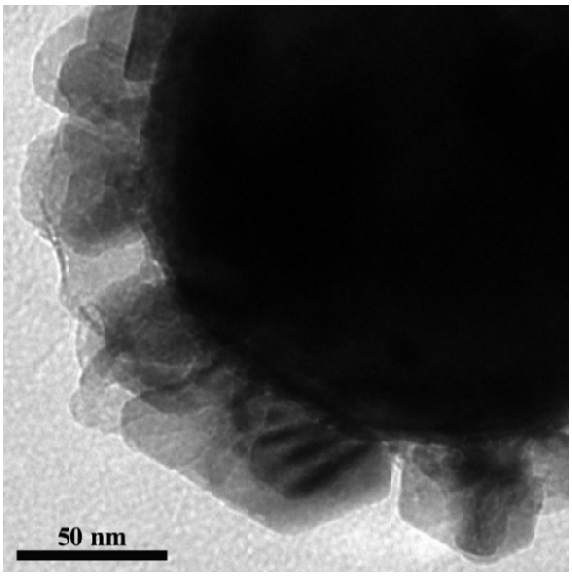

(a)

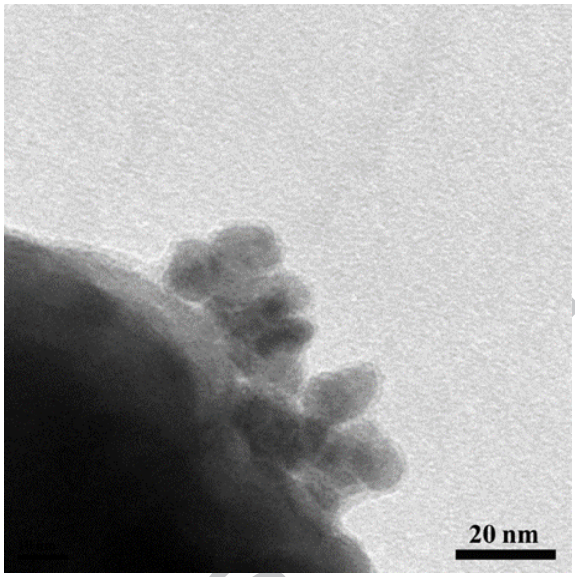

(b)

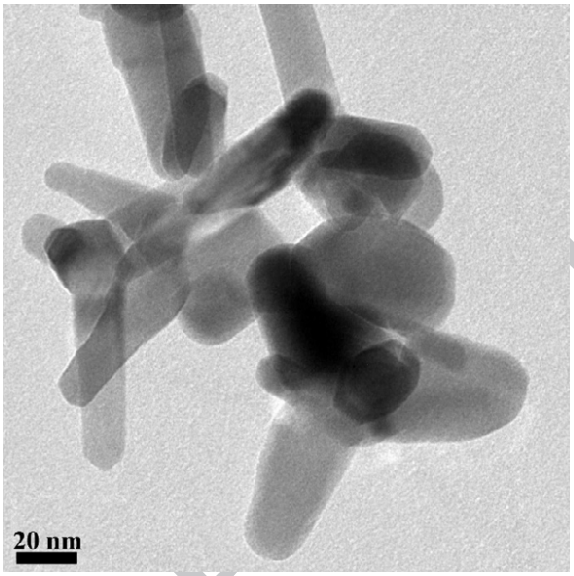

(c)

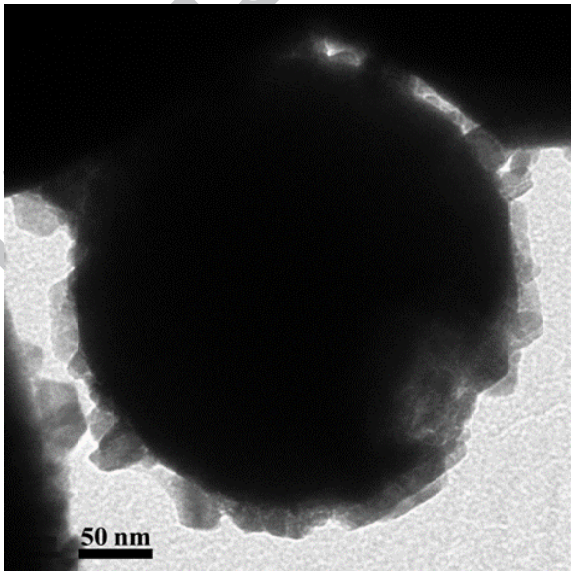

(d)

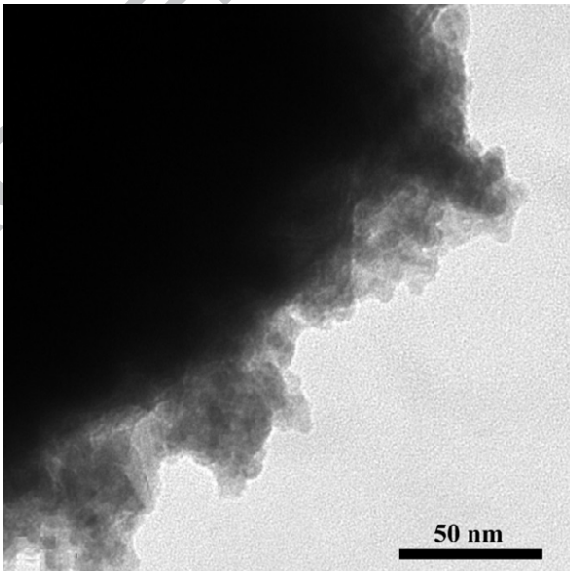

(e)

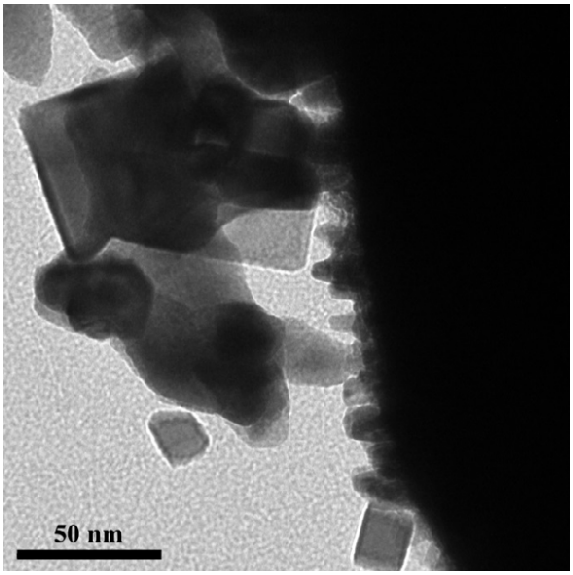

(f)

Fig. 1. TEM micrographs of NPs listed in Table 1: a – Z4, b – Z5, c – Z7, d – Z10, e - Z14, and f – Z15.

3.2. X-ray diffraction

X-ray diffraction patterns of NPs showed reflections: (i) hexagonal Zn lattice closed to JCPDS file 04-0831 with unit-cell parameters of ranged from a = 0.2653 nm to a = 0.2665 and from c = 0.4925 nm to c = 0.4949 (Fig. 2 and inset); (ii) hexagonal zinc oxide (JCPDS, 74-0534) with unit-cell parameters a = 0.3250 nm and c = 0.5207 nm which (with acceptable accuracy) varied slightly from sample to sample. On the inset of Fig.2 on the example of Zn [34] reflection it can be noted that NPs Z8 demonstrated a high level of crystallinity (a reflection related with Cu $K_{\alpha 2}$ radiation is visible) and NPs Z4 – a low one. The percentages of the crystal phases, evaluated at resolving power of the full profile analysis, are presented in the Table 1 together with the principal controlled parameters of the nanoparticle preparation process: metallic zinc feed rate as well as inert and oxidant gas flow rates.

As shown in Table 1, the zinc oxide content (V_{xrd}) of all our samples did not exceeded 65 %. It is worth pointing out that crystal structure, phase composition and other characteristics were determined after prolonged storage of NPs in air, since as-prepared particles demonstrated a number of changes in their properties during an ageing at room temperature [28]. Therefore, we have failed to determine uniquely the composition of plate-like nanoparticles on the surface of Zn particles with by XRD, it is reasonable to assume that the former particles consisted predominantly of ZnO what be verified later.

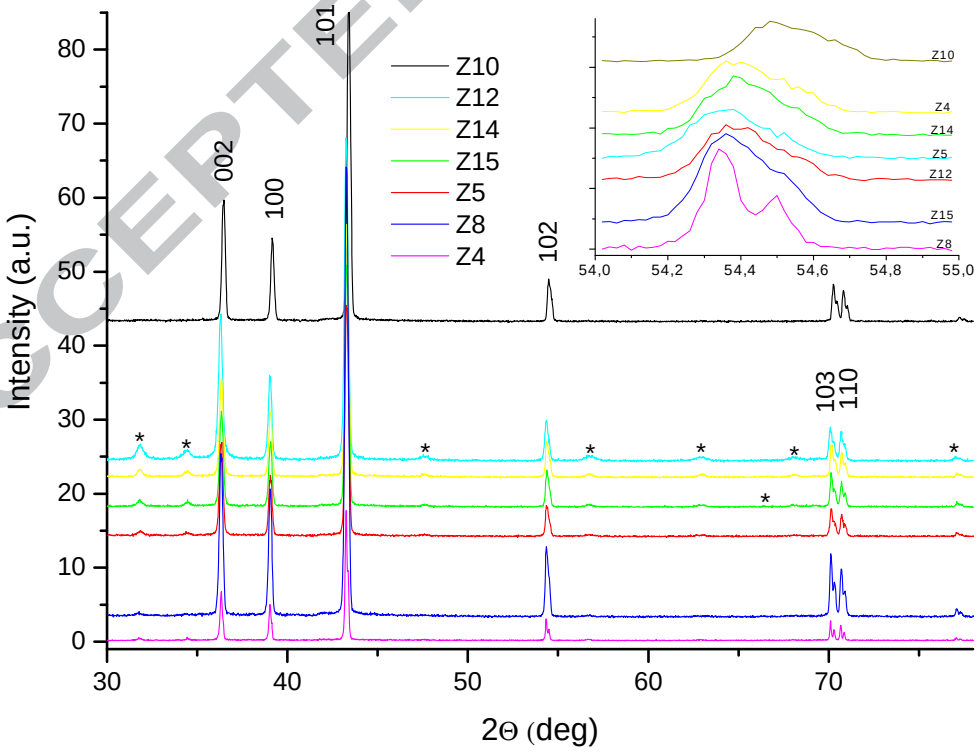

Fig. 2. XRD patterns of NPs. The numbers of the curves corresponds to the numbers of NPs in Table 1. Miller indices, refers to the reflections from zinc and those from zinc oxide, are marked by asterisks.

3.3 Optical characterization of NPs

UV-vis absorption spectra

The UV-vis absorption spectra of different NPs at RT presented in Fig. 3a. A sharp peak has been founded in the range of 353-367 nm compared with 368–373 nm [37], where it was determined as a characteristic peak of the wurtzite hexagonal phase ZnO [50, 51]. The absorption peaks are “blue shifted” from the bulk ZnO (368.5 nm), probably, due to the weak quantum confinement effect [37].

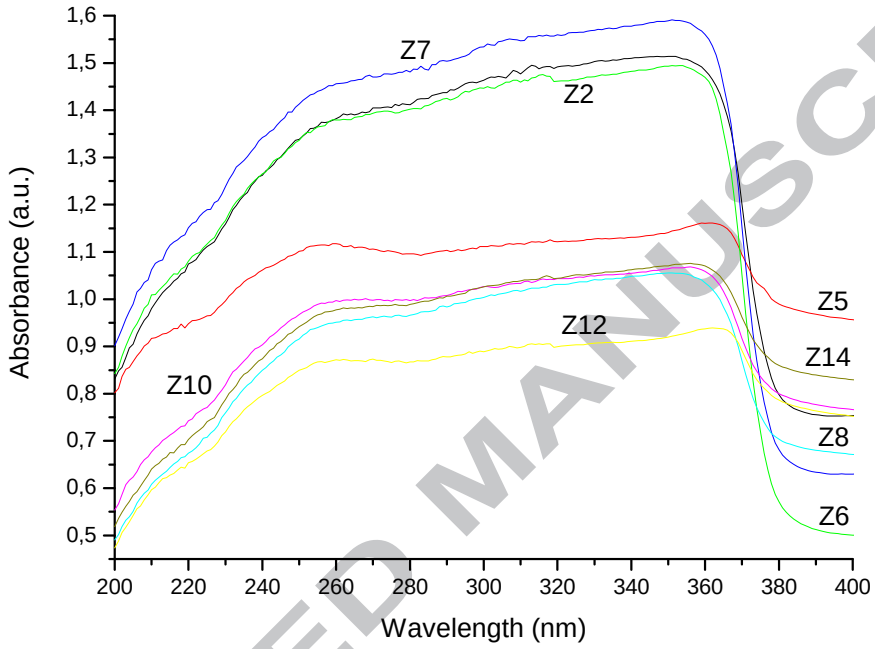

(a)

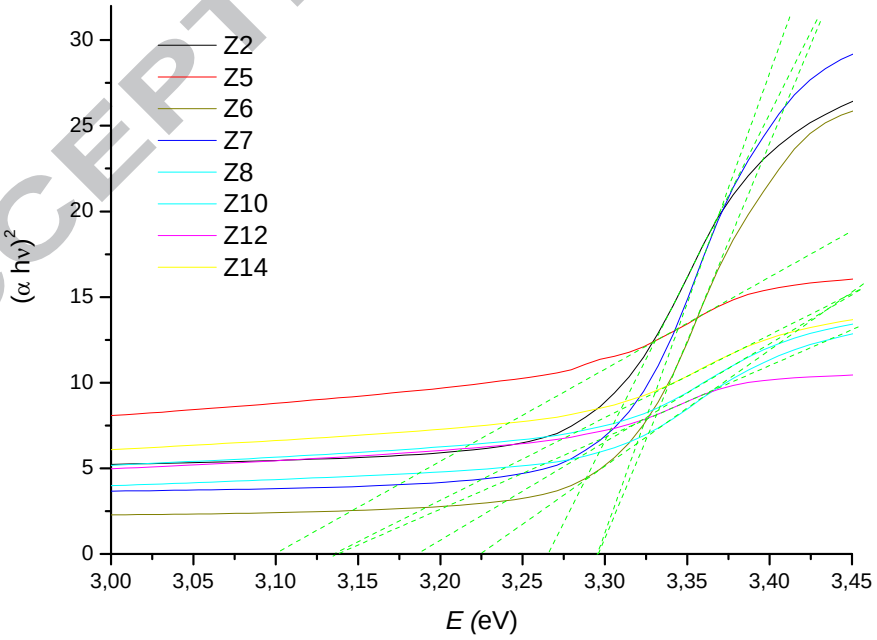

(b)

Fig. 3. (a) UV-vis absorption spectra of NPs at room temperature. (b) Plots of $(\alpha h\upsilon)^2$ vs. $h\upsilon$ for the NPs. The numbers of curves corresponds to the numbers of NPs in Table 1.

The optical band gap energy (E_g) can be estimated from absorption coefficient (α) using the Tauc relation [52]:

$$\alpha h\upsilon = A(h\upsilon - E_g)^q,$$

where A is a constant that depends from the transition probability, $h\upsilon$ is the energy of an incident photon, and q is an index that characterizes the optical absorption process. It is well known that direct and indirect band gap energy for the semiconductor nanostructures can be obtained from the intersection of linear fits of $(\alpha h\upsilon)^{1/q}$ vs. $h\upsilon$ plots for q = 0.5 [53], as ZnO is the direct band gap semiconductor material. Fig. 3b (based on Fig. 3a) shows the $(\alpha h\upsilon)^2$ vs. $h\upsilon$ plots for some of NPs. All the estimated E_g results for NPs, which based on Fig. 3b, showed in Table 1. The band gap of NPs has been calculated from the UV–vis spectra and varies in the range of 3.10–3.30 eV. It was smaller in comparison to the standard bulk ZnO (~ 3.37 eV) [51] due to the high carrier concentration [54].

FT-IR spectra

FT-IR is a powerful technique to find out the information about the chemical bonding in the material, identification of the elemental constituents of material and getting the supplementary information from XRD and TEM [55]. Infrared studies were performed aiming to ascertain the metal-oxygen and nature of NPs. Metal oxides generally give absorption bands below 1000 cm^{-1} arising from the inter-atomic vibrations [56]. FT-IR spectra of NPs shown in Fig. 4a. All the prepared samples shows vibrations in the region of 385–690 cm^{-1}, which are assigned to the metal-oxygen stretching vibration and no broad peaks has been observed at 1600–1640 and 3100–3600 cm^{-1} due to the presence of water after hydration by exposure the samples in open air [56]. In order to determine exact positions of the bands, IR band in the region of 400–700 cm^{-1} shown in Fig. 4b. As shown, the entire NPs can divided into three different groups depending on their average particle sizes. The first group: the NPs Z12, Z10, Z14 (300-430 nm) demonstrated broad bands at 450, 490 and 560 (I) cm^{-1}. The second group: the NPs Z8, Z15, Z1 (610-760 nm) showed bands at 450, 490, 540 (II) cm^{-1}. Finally, the third group: the NPs Z7, Z 6, Z2 (480-600 nm) observed peaks at 450, 490, 520 (III) cm^{-1}. All of these bands can be fitted by using Gaussian to the three bands A_1, A_2 and A_3 [57] (vertical reference lines). According to Burstein and Bundesmann [58, 59], band A_1 around of 435-450 cm^{-1} corresponds to the E_1 transversal-optical (TO) mode. Bands which are centered at 490 cm^{-1} (A_2) and 520-560 cm^{-1} (A_3) are surface phonon modes, which normally appears when NPs are smaller than the incident IR wavelength radiation [59]. The IR bands, corresponds to Zn, showing a variation in the vibrational frequencies with decrease in the average particle sizes. The

shift in the band position (indicated by an arrow) may appear due to the structural changes induced by the Zn unit-cell volume changing because of Zn–O–Zn network was perturbed at the Zn/ZnO interface [28] what be discussed later.

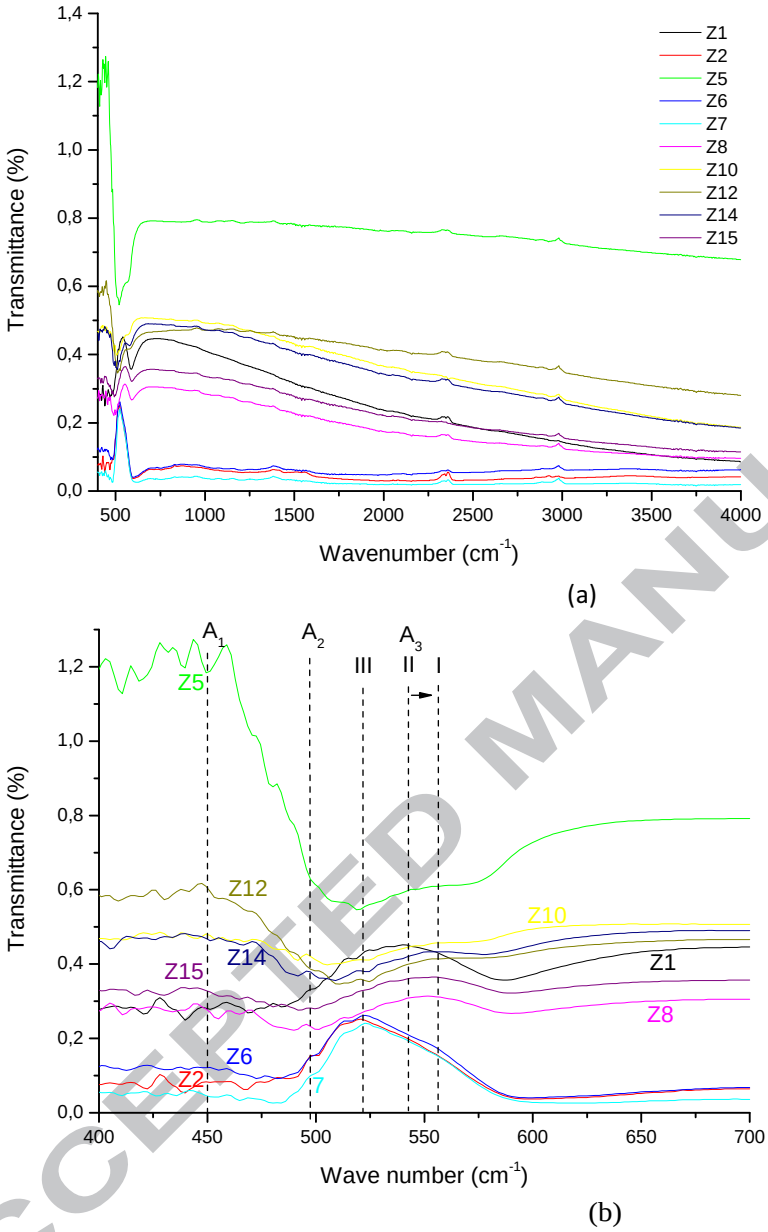

Fig. 4. (a) FT-IR spectra of NPs. (b) IR band in the range of 400–700 cm^{-1}. The numbers of curves corresponds to the numbers of NPs in Table 1.

Raman spectra

It is well-known that ZnO has a wurtzite structure, with two atoms per primitive cell and the group theory predicts four Raman active modes, $A_1 + E_1 + 2E_2$ [60]. Both A_1 and E_1 modes are infrared active, polar, and thus splitting out into the longitudinal-optical (LO) and transversal-optical (TO) components. E_2 modes of E_2^{high} and E_2^{low} are nonpolar and Raman active correspond to the vibrations of oxygen atoms and Zn sub-lattice, respectively [61]. Fig. 5 shows Raman spectra some of our NPs. In this figure, it may see

the large-sized NPs (Z3, Z8) exhibit large Raman intensity because of the density of defect in the Zn/ZnO interface enhanced due to the co-adhesion of Zn and ZnO nanoparticles. The reason for the small-sized NPs (Z6, Z7) causing Raman intensity to decrease properly related with the capped structure vanishing mentioned above. The E_2^{high} mode, located at ~ 436 cm^{-1} in the Raman spectrum of pure ZnO [60], goes through significant changes, as it was shown in Fig. 5. For large-sized NPs this Raman mode, assigned to the oxygen vibrations [60], is more relative intensive than for small-sized NPs. This fact is in accordance with above NPs morphology change when their d_{BET} decrease. A pronounced asymmetry of E_2^{high} peak may be attributed to the lattice disorder, as well as to the non-harmonic phonon–phonon interactions [60]. Therefore, the Raman signals features may be related to the real morphology of Zn/ZnO interface in the NPs. The fact is, that E^{high} Raman mode, originated from the oxygen vibrations in the ZnO crystal lattice, is more affected by interstitial Zn than the E^{low} mode, ascribed to the Zn sublattice vibrations [62], suggests that the oxygen defects, probably, dominate on the ZnO side of the interface.

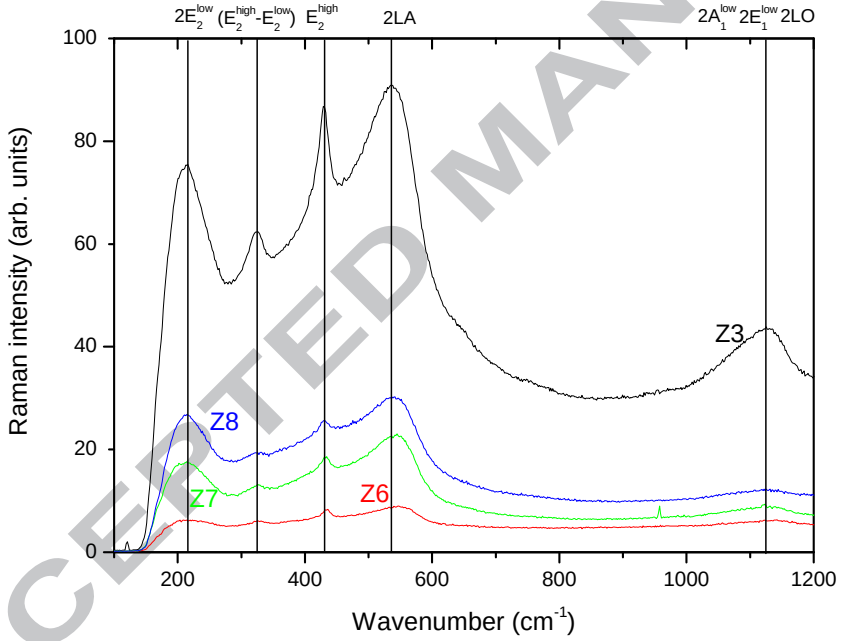

Fig. 5. Raman spectra of NPs. The numbers of the curves correspond to the numbers of NPs in Table 1.

3.4 XPS results

The surface composition and chemical states can be determined by means of XPS spectrum according to the characterizing binding energies of the different elements on material surfaces. Fig. 6a shows a survey XPS spectrum from the NPs, indicating the following elements presence: Zn, O and adventitious C. No contaminants from the nanoparticle synthesis were detected on the sample surface. In our samples, residual amounts of adventitious carbon and carbonyl compounds were unavoidable due to their exposure to air [63, 64].

The XPS spectra of the Zn-2p core level regions of some NPs seen on Fig. 6b. The NPs displays a doublet at about 1022 and 1045 eV (vertical reference lines), corresponding to the Zn-$2p_{3/2}$ and $2p_{1/2}$ core levels [65]. The first peak is attributed to Zn^{2+} ions in the oxygen-deficient ZnO matrix [66]. Moreover, the all of Zn $2p_{3/2}$ XPS peaks are sharp. Thus, it can be confirmed, that Zn element exists mainly in the form of Zn^{2+} on the samples surfaces [67] i.e. ZnO really form the capped area of our NPs.

The asymmetric peak was observed in the O-1s region (Fig. 6c, normalized view). Assuming that the O-1s emission is composed by two contributions, XPS line was fitted with the Origin 9.1 software by using two Gauss profile functions [67], including linear background [68, 69].

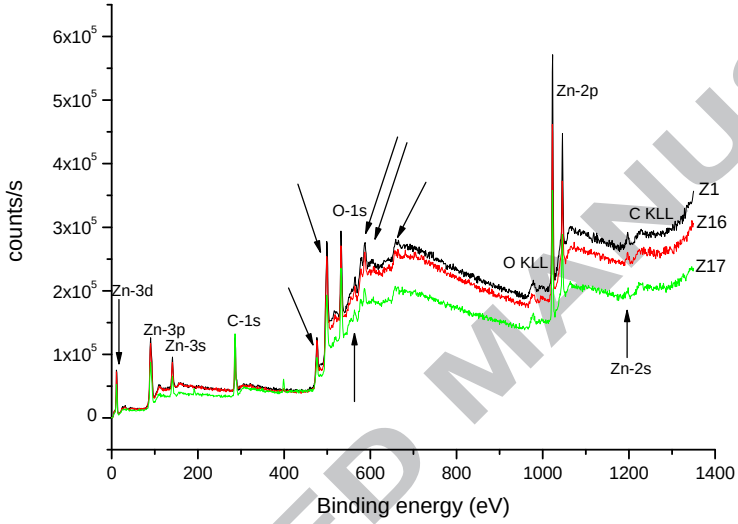

(a)

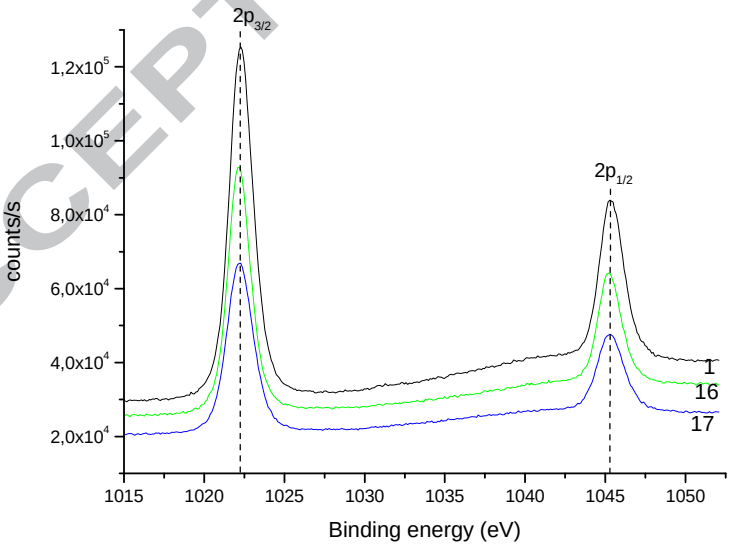

(b)

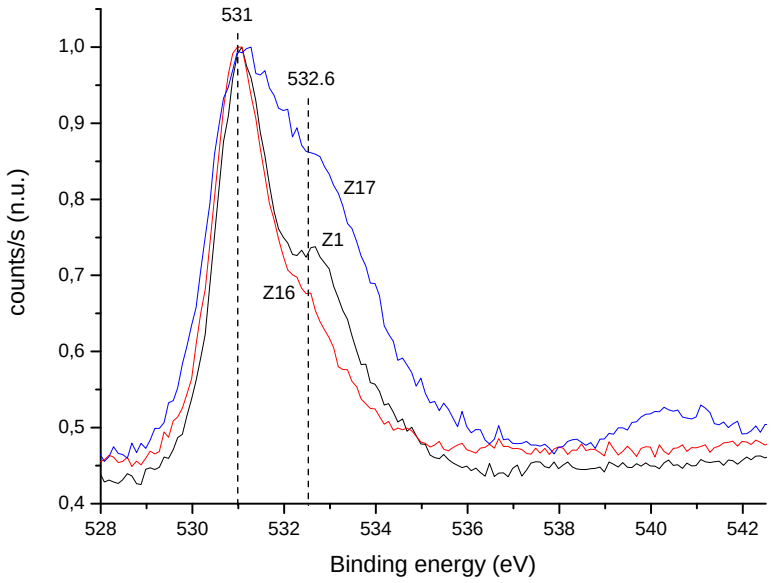

(c)

Fig. 6. (a) Survey XPS spectrum from NPs. (b) XPS spectra of the Zn-2p core level regions. (c) XPS spectra of the O-1s core level regions. The numbers of the curves correspond to the numbers of NPs in Table 1.

Table 2
Curve fitting results of NPs O-1s XPS spectra

Sample ID	E_b (eV)	FWHM (eV)	%
Z1	531.0	1.12	37
	532.4	2.76	63
Z16	530.9	1.14	44
	532.6	2.63	56
Z17	530.9	1.15	32
	532.6	2.95	68

These two peaks are attributed to the O_2^- ions in the normal wurtzite structure of ZnO powder [70] and O_2^- ions in the oxygen-deficient regions within the ZnO (defective ZnO_x) matrix [66, 67], respectively. The last component could be attributed to the presence of partially reduced ZnO (ZnO_x) [71] (oxidized Zn) or $Zn(OH)_2$ at the Zn/ZnO interface. In the latter case, the FWHM value may be broaden because of the amorphous nature of this material [68]. Due to that, no obvious particle size dependence of the peaks parameters were found in our NPs. The determined binding energies E_b, full width at half-maximum (FWHM) and percentage values of the fitted components are listed in Table 2. As it is clearly seen from Fig. 6c and Table 2 NPs Z17 demonstrated a pronounced defective surface state compared with the others NPs.

3.5 Magnetic measurements

Magnetic measurements showed that NPs have ferromagnetic hysteresis loops at room temperature [28]. The results of magnetization measurements for some NPs (σ, *vs.* applied

magnetic field, *H*) presented in Fig. 7 shows that most of the NPs exhibits weak ferromagnetic moment, accompanied by diamagnetic behavior of bulk Zn with magnetic susceptibility, which does not exceeded the known value -1.4×10^{-7} cm^3/g [72]. NPs Z3, Z15 and Z4 exhibit well-defined ferromagnetic behavior with an appropriate saturation magnetization. All of the hysteresis loops exhibit soft-magnetic behavior with coercivity ranged within 65-118 Oe. In Table 1 one of the basic characteristics of hysteresis loops - specific maximum magnetization σ_{max} is presented. It is worth pointing out that the maximum magnetization of the nanoparticles is obviously independent from their average particle size and ZnO content. The highest room temperature saturation magnetization obtained in this study was 0.27 emu/g (Z17), which was found to be a higher value in comparison to the literature one (from 6×10^{-4} to 6×10^{-3} emu/g) for non-doped ZnO nanoparticles of various sizes in the range of 4–500 nm [19, 22, 26, 39, 45, 73-75]. Higher values of up to 0.62 emu/g were reported for the ZnO nanofilms, but significant error was obviously possible in the thin films masses determination. Moreover, reducing the saturation magnetization of our best sample to the weight percentage of ZnO, we obtained the value up to 18 emu/g.

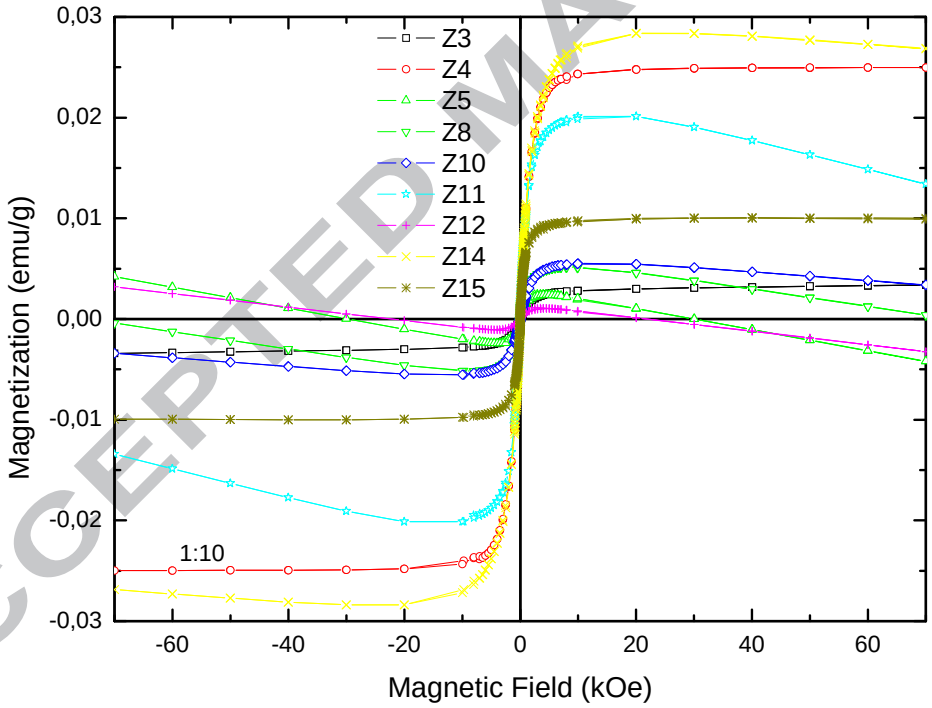

Fig. 7. Ferromagnetic hysteresis loops of some NPs from Table 1. The numbers of curves corresponds to the numbers of NPs in Table 1.

One of the main goals in this study was to find out whether the maximum saturation magnetization of nanoparticles depending from primary parameters of NPs which has not been established unequivocally [76] shows a clear correlations between defect-related emissions [77], photoluminescence [78], electron-spin resonance [79] and the

magnetization data of ZnO are essentially secondary characteristics. Fig. 8 shows dependence of the maximum magnetization of NPs from the unit-cell volume crystal lattice of Zn (V) for the different samples from Table 1. The magnetization was seen to rise up sharply as V decreases relative to that of the bulk Zn ($V_b = 3.5151 \times 10^{-2}$ nm^3) by $\Delta V = V_b - V = 1.8 \times 10^{-4}$ nm^3, that is of about 0.51% of V_b. It can be interpreted as an evidence that the magnetic order development is related to the presence of vacancies, such as V_{Zn}, in the crystal lattice of the Zn nanoparticles, whose role in RTFM was reported earlier for undoped ZnO [80, 81]. V_{Zn}^{-} and V_{ZnO}^{-} (the negatively charged ZnO pair vacancy) are proposed as possible sources of magnetic moment in ferromagnetic ZnO films [25]. These vacancies can trap one or two electrons and their charge transition levels lie in the band gap. The ferromagnetic moment arises from electrons trapped at negatively charged vacancies in an *n*-type ZnO. A one-band Hubbard Hamiltonian describes trapped electrons where the Hubbard parameter is the effective electron-electron repulsion for a pair of electrons in a vacancy. Ferromagnetism as known to exist in the Hubbard model applied to periodic three-dimensional lattices, provided the Hubbard parameter exceeds the defect bandwidth and the filling is away from half or complete filling. Hybrid and local-density approximation DFT calculations are used to evaluate Hubbard parameters for electrons trapped in defects in ZnO [25]. They also used to calculate magnetic exchange couplings of well-separated, singly negatively charged defects, which induced by a conduction band electron. Strong ferromagnetic coupling between defects is found in these total-energy calculations over a range exceeding one nm when the defects have a large, positive Hubbard parameter value, which may be large enough to support a Hubbard model for ferromagnetism.

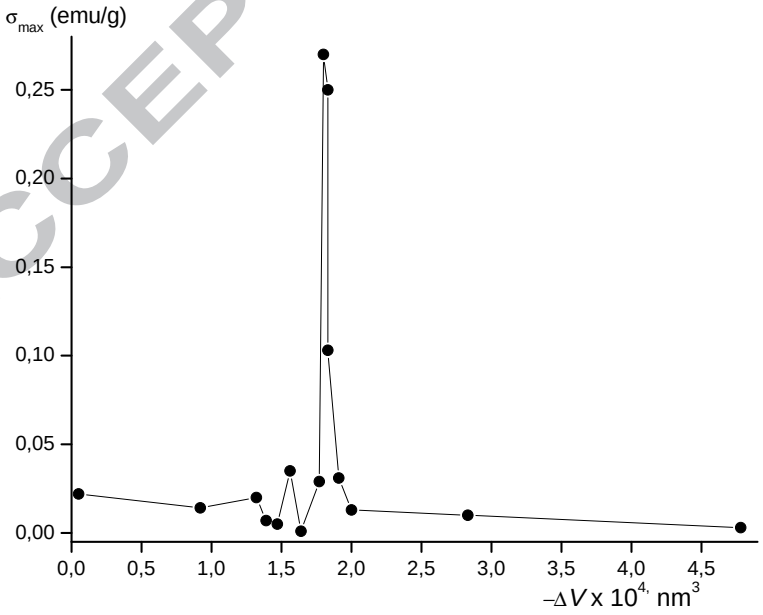

Fig. 8. Maximum magnetization of NPs *vs.* unit-cell volume change in Zn crystal lattice.

For magnetization to reach a value comparable to those observed in the our experiments, the defect density in the order of 1 at % was necessary in ZnO [25]. This was found comparable to the decrease in V observed in our NPs. The following results, however, should be taken into account. In principle, our NPs, consisting primarily of pure Zn, cannot be imperfect throughout the volume, because of the intense diffusion processes during its crystallization. Most likely, local magnetic moments develops in the thin layers at the interface between two phases in the Zn particles—in their bulk and ZnO nanoparticles in their surface layer—leading to the formation of highly imperfect structure [23], in which long-range magnetic interactions are possible. In such an imperfect structure, among oxygen vacancies in various charge states only singly charged oxygen vacancies offers the possibility of quantum localization effect, owing to the elimination of paired electron spins in doubly charged and neutral oxygen vacancies.

Concerning to the optical properties, the situation is not so obvious. UV-vis data demonstrated that the band gap for NPs Z7 is essentially larger than the gap for Z14. It seems to be that in the last NPs large amounts of charged species are present at the energy levels of local vacancies are below the upper edge of the gap. The diminishing of V value in this case supports this suggestion. However, maximum magnetization for the NPs Z14 is lower than for the Z7 ones. It is possible, that for the NPs Z14 no percolation threshold of the traps interaction within the Zn/ZnO interface was reached and σ reaches not its maximum value. Furthermore, it can be noted that near this threshold the NPs are exhibit a broadening in the maximum and ‘blue shifts’ in IR transmittance within the region of 500-600 cm^{-1} (cf. NPs Z14 and Z1 curves in Fig. 4a). The Raman spectra of NPs (Fig. 5) pointing out the predominant role of the Zn vacancies in magnetic properties from the Zn side of Zn/ZnO interface rather than oxide ones from the counterpart side.

In our NPs, V_O of singly charged oxygen vacancies are also important for the development of local magnetic states [19] and the corresponding magnetic interaction in the system . Since the surface composition and chemical states determined by means of XPS spectrum characterized by the binding energies of oxygen on the particles surfaces, in NPs Z16, Z1, Z17 the progressive broadening of the peaks takes place accompanied by the maximum magnetization enhancement (Figs. 6, 7). This, however, does not rule out that other defect species, such as above-mentioned cation vacancies [16] that may be responsible for the long-range ferromagnetic ordering. Most likely, both types of vacancies are contributing to RTFM. It is reasonable to assume that the interfacial region has the highest concentration of all the vacancies, and its structure transforms to the ferromagnetic “grain-boundary foam” [82]. The nature of ferromagnetic interaction between the local magnetic moments (or vacancy clusters [74]) is not quite obvious, even though the issue has been

addressed using first-principles calculations [83, 84]. Under such conditions, studies of the thermal stability of RTFM and its time variation in Zn/ZnO NPs may be helpful [28].

4. Conclusions

Zinc aerosol-generated particles ranging in average size from 42 to 760 nm and capped with zinc oxide nanoparticles of about 10-30 nm in sizes can be prepared by levitation-jet synthesis through condensation of zinc metal vapor in an inert-gas flow under some oxidation conditions. XRD, UV-vis, FT-IR, Raman and XPS studies demonstrated the strong-defective structure of the Zn/ZnO NPs interface.

The synthesized materials are ferromagnetic with saturation magnetization up to 0.27 emu/g and coercive force up to 200 Oe. The saturation magnetization of NPs as a function of unit-cell volume of crystal lattice of Zn has a maximum in the range of values, where material is looser than bulk zinc. Such behavior may be interpreted in terms of the defect structure of the Zn/ZnO interfacial layer, containing Zn and O vacancies, whose concentration and degree of mutual interactions can be controlled by varying NPs preparation conditions.

Acknowledgments

The authors acknowledge financial support from the Russian Foundation of Basis Research (research project No. 13-03-12407) and the Presidium Russian Academy of Sciences (Program No. 26).

References

[1] A. Lajn, M. Schmidt, H. von Wenckstern, M. Grundmann, Transparent Rectifying Contacts for Visible-Blind Ultraviolet Photodiodes Based on ZnO, Journal of Elec Materi, 40 (2011) 473-476.
[2] R. Jose, V. Thavasi, S. Ramakrishna, Metal Oxides for Dye-Sensitized Solar Cells, Journal of the American Ceramic Society, 92 (2009) 289-301.
[3] T. Minami, T. Miyata, K. Ihara, Y. Minamino, S. Tsukada, Effect of ZnO film deposition methods on the photovoltaic properties of ZnO–Cu2O heterojunction devices, Thin Solid Films, 494 (2006) 47-52.
[4] Z. Zang, A. Nakamura, J. Temmyo, Single cuprous oxide films synthesized by radical oxidation at low temperature for PV application, Opt. Express, 21 (2013) 11448-11456.
[5] Z. Zang, A. Nakamura, J. Temmyo, Nitrogen doping in cuprous oxide films synthesized by radical oxidation at low temperature, Materials Letters, 92 (2013) 188-191.
[6] S.J. Pearton, F. Ren, p-type doping of ZnO films and growth of tenary ZnMgO and ZnCdO: application to light emitting diodes and laser diodes, International Materials Reviews, 59 (2014) 61-83.
[7] L.Y.-P. Xu Yun, Jin Lu, Ma Xiang-Yang, Yang De-Ren, Low-threshold electrically pumped ultraviolet random lasing from ZnO film prepared by pulsed laser deposition, Acta Phys. Sin, 62 (2013) 84207-084207.
[8] Y.-C. Shen, C.-H. Yang, S.-W. Chen, S.-H. Wu, T.-L. Yang, J.-J. Huang, IGZO thin film transistor biosensors functionalized with ZnO nanorods and antibodies, Biosensors and Bioelectronics, 54 (2014) 306-310.
[9] M. Hjiri, L. El Mir, S.G. Leonardi, A. Pistone, L. Mavilia, G. Neri, Al-doped ZnO for highly sensitive CO gas sensors, Sensors and Actuators B: Chemical, 196 (2014) 413-420.

[10] V.S. Khomchenko, N.N. Roshchina, L.V. Zavyalova, V.V. Strelchuk, G.S. Svechnikov, N.P. Tatyanenko, V.L. Gromashevskii, O.S. Litvin, E.A. Avramenko, B.A. Snopok, Structure and the emission and piezoelectric properties of MOCVD-grown ZnS, ZnS-ZnO, and ZnO films, Tech. Phys., 59 (2014) 93-101.
[11] M. Yuste, R.E. Galindo, O.M. Sacristán, I. Mínguez-Bacho, R. Sonia, M. Hernández-Vélez, O. Sánchez, Structural and optical characterization of nanostructured ZnO grown on alumina templates, Materials Research Express, 1 (2014) 045028.
[12] W. Zhang, J. Zhao, Z. Liu, Z. Liu, Structural, optical and magnetic properties of $Zn_{1-x}Fe_xO$ powders by sol–gel method, Applied Surface Science, 284 (2013) 49-52.
[13] M. Venkatesan, C.B. Fitzgerald, J.M.D. Coey, Unexpected magnetism in a dielectric oxide, Nature, 450 (2004) 630.
[14] J.M. Coey, M. Venkatesan, C.B. Fitzgerald, Donor impurity band exchange in dilute ferromagnetic oxides, Nature materials, 4 (2005) 173-179.
[15] N.H. Hong, A. Barla, J. Sakai, N.Q. Huong, Can undoped semiconducting oxides be ferromagnetic?, physica status solidi (c), 4 (2007) 4461-4466.
[16] M. Khalid, M. Ziese, A. Setzer, P. Esquinazi, M. Lorenz, H. Hochmuth, M. Grundmann, D. Spemann, T. Butz, G. Brauer, W. Anwand, G. Fischer, W. Adeagbo, W. Hergert, A. Ernst, Defect-induced magnetic order in pure ZnO films, Physical Review B, 80 (2009) 035331.
[17] Q. Xu, H. Schmidt, S. Zhou, K. Potzger, M. Helm, H. Hochmuth, M. Lorenz, A. Setzer, P. Esquinazi, C. Meinecke, M. Grundmann, Room temperature ferromagnetism in ZnO films due to defects, Applied Physics Letters, 92 (2008) 082508.
[18] Q. Wang, Q. Sun, G. Chen, Y. Kawazoe, P. Jena, Vacancy-induced magnetism in ZnO thin films and nanowires, Physical Review B, 77 (2008) 205411.
[19] D. Gao, Z. Zhang, J. Fu, Y. Xu, J. Qi, D. Xue, Room temperature ferromagnetism of pure ZnO nanoparticles, Journal of Applied Physics, 105 (2009) 113928.
[20] S. Majumder, D. Paramanik, A. Gupta, S. Varma, Observation of magnetic domains in undoped ZnO grains at room temperature, Applied Surface Science, 256 (2009) 513-516.
[21] Y. Li, R. Deng, B. Yao, G. Xing, D. Wang, T. Wu, Tuning ferromagnetism in $Mg_xZn_{1-x}O$ thin films by band gap and defect engineering, Applied Physics Letters, 97 (2010) 102506.
[22] X. Zhang, Y.H. Cheng, L.Y. Li, H. Liu, X. Zuo, G.H. Wen, L. Li, R.K. Zheng, S.P. Ringer, Evidence for high granular films mediated by native point defects, Physical Review B, 80 (2009) 174427.
[23] A.L. Schoenhalz, J.T. Arantes, A. Fazzio, G.M. Dalpian, Surface magnetization in non-doped ZnO nanostructures, Applied Physics Letters, 94 (2009) 162503.
[24] D. Kim, J.-h. Yang, J. Hong, Ferromagnetism induced by Zn vacancy defect and lattice distortion in ZnO, Journal of Applied Physics, 106 (2009) 013908.
[25] A. Chakrabarty, C.H. Patterson, Defect trapped electrons and ferromagnetic exchange in ZnO, Phys. Rev. B: Condens. Matter Mater. Phys., 84 (2011) 054441.
[26] W. Liu, W. Li, Z. Hu, Z. Tang, X. Tang, Effect of oxygen defects on ferromagnetic of undoped ZnO, Journal of Applied Physics, 110 (2011) 013901.
[27] S. Shit, T. Kamilya, P.K. Samanta, A novel chemical reduction method of growing ZnO nanocrystals and their optical property, Materials Letters, 118 (2014) 123-125.
[28] M.V. Kuznetsov, Y.G. Morozov, O.V. Belousova, D. Ortega, Ferromagnetic Zn/ZnO Nanoparticles, Inorganic Materials, 50 (2014) 369-378.
[29] B. Yao, H. Shi, H. Bi, L. Zhang, Optical properties of ZnO loaded in mesoporous silica, Journal of Physics: Condensed Matter, 12 (2000) 6265.
[30] S. Das, K. Bhattacharjee, S. Maitra, G.C. Das, Effect of oxygen partial pressure on the photoluminescence properties of sol–gel synthesized nano-structured ZnO thin films, Thin Solid Films, 550 (2014) 65-70.
[31] G.-Q. Tang, Y. Xiong, L.Z. Zhang, G.-L. Zhang, Novel long-lifetime photoluminescence of nanosized ZnO included in the mesoporous MCM-41, Chemical Physics Letters, 395 (2004) 97-102.
[32] I. Lorite, L. Villaseca, P. Díaz-Carrasco, M. Gabás, J.L. Costa-Krämer, Doping, carriers and intergrain

fields in ZnO films: An impedance and confocal Raman spectroscopy study, Thin Solid Films, 548 (2013) 657-660.
[33] S.S. Xiao, L. Zhao, Y.H. Liu, J.S. Lian, Nanocrystalline ZnO films prepared by pulsed laser deposition and their abnormal optical properties, Applied Surface Science, 283 (2013) 781-787.
[34] K.S. Babu, A.R. Reddy, K.V. Reddy, Controlling the size and optical properties of ZnO nanoparticles by capping with SiO_2, Materials Research Bulletin, 49 (2014) 537-543.
[35] H. Rashidi, A. Ahmadpour, F.F. Bamoharram, S.M. Zebarjad, M.M. Heravi, F. Tayari, Controllable one-step synthesis of ZnO nanostructures using molybdophosphoric acid, Chemical Papers, 68 (2014) 516-524.
[36] E. Solati, L. Dejam, D. Dorranian, Effect of laser pulse energy and wavelength on the structure, morphology and optical properties of ZnO nanoparticles, Optics & Laser Technology, 58 (2014) 26-32.
[37] N. Rajamanickam, S. Rajashabala, K. Ramachandran, On the structural and optical properties of nano-ZnO and its morphologies, Journal of Luminescence, 146 (2014) 226-233.
[38] M.Y. Gen, A.V. Miller, A levitation method for producing ultrafine metal powders Poverkhnost Fiz. Khim. Mekh., (1983) 150-154.
[39] X. Xu, C. Xu, J. Dai, J. Hu, F. Li, S. Zhang, Size Dependence of Defect-Induced Room Temperature Ferromagnetism in Undoped ZnO Nanoparticles, The Journal of Physical Chemistry C, 116 (2012) 8813-8818.
[40] L.Y. Li, Y.H. Cheng, X.G. Luo, L. Hui, G.H. Wen, R.K. Zheng, S.P. Ringer, Room-temperature ferromagnetism and the scaling relation between magnetization and average granule size in nanocrystalline Zn/ZnO core–shell structures prepared by sputtering, Nanotechnology, 21 (2010) 145705.
[41] Y.G. Morozov, O.V. Belousova, M.V. Kuznetsov, D. Ortega, I.P. Parkin, Electric field-assisted levitation-jet aerosol synthesis of Ni/NiO nanoparticles, J. Mater. Chem., 22 (2012) 11214-11223.
[42] D. Ortega, M.V. Kuznetsov, Y.G. Morozov, O.V. Belousova, I.P. Parkin, Phase, size and shape controlled formation of aerosol generated nickel and nickel oxide nanoparticles, Journal of Alloys and Compounds, 579 (2013) 495-501.
[43] M.A. Garcia, E. Fernandez Pinel, J. de la Venta, A. Quesada, V. Bouzas, J.F. Fernández, J.J. Romero, M.S. Martín González, J.L. Costa-Krämer, Sources of experimental errors in the observation of nanoscale magnetism, Journal of Applied Physics, 105 (2009) 013925.
[44] D. Ortega, M.V. Kuznetsov, Y.G. Morozov, O.V. Belousova, I.P. Parkin, Thermal relaxation and collective dynamics of interacting aerosol-generated hexagonal NiFe2O4 nanoparticles, Physical Chemistry Chemical Physics, 15 (2013) 20830-20838.
[45] M.A. Garcia, J.M. Merino, E. Fernández Pinel, A. Quesada, J. de la Venta, M.L. Ruı´z Gonza´lez, G.R. Castro, P. Crespo, J. Llopis, J.M. Gonza´lez-Calbet, A. Hernando, Magnetic properties of ZnO nanoparticles, Nano Letters, 7 (2007) 1489-1494.
[46] A. Hernando, M.A. Garc´ıa, Magnetism induced by capping of non-magnetic ZnO nanoparticles, Journal of Nanoparticle Research, 13 (2011) 5595-5602.
[47] A. Hernando, P. Crespo, M. Angel Garcı´a, M. Coey, A. Ayuela, P.M. Echenique, Revisiting magnetism of capped Au and ZnO nanoparticles: Surface band structure and atomic orbital with giant magnetic moment, Physica Status Solidi B 248 (2011) 2352–2360.
[48] D. Ortega, J.C. Herna´ndez-Garrido, C. Blanco-Andujar, J.S. Garitaonandia, Suppression and enhancement of the ferromagnetic response in Fe-doped ZnO nanoparticles by calcination of organic nitrogen, phosphorus, and sulfur compounds, Journal of Nanoparticle Research 15 (2013) 2120-2130.
[49] O. Lupan, L. Chow, G. Chai, A single ZnO tetrapod-based sensor, Sensors and Actuators B: Chemical, 141 (2009) 511-517.
[50] R. Wahab, S.G. Ansari, Y.S. Kim, H.K. Seo, G.S. Kim, G. Khang, H.-S. Shin, Low temperature solution synthesis and characterization of ZnO nano-flowers, Materials Research Bulletin, 42 (2007) 1640-1648.
[51] R. Wahab, S.G. Ansari, Y.-S. Kim, H.-K. Seo, H.-S. Shin, Room temperature synthesis of needle-shaped ZnO nanorods via sonochemical method, Applied Surface Science, 253 (2007) 7622-7626.

[52] J. Zhang, D. Gao, G. Yang, Z. Zhu, J. Zhang, Z. Shi, Study on Synthesis and Optical Properties of ZnO Hierarchical Nanostructures by Hydrothermal Method, International Journal of Material and Mechanical Engineering, 1 (2012) 38-43.
[53] D.Q. Gao, Z.H. Shi, Y. Xu, J. Zhang, G.J. Yang, J.L. Zhang, X.H. Wang, D.S. Xue, Synthesis, Magnetic Anisotropy and Optical Properties of Preferred Oriented Zinc Ferrite Nanowire Arrays, Nanoscale Research Leters, 5 (2010) 1289-1294.
[54] T.G. Venkatesha, Y. Arthoba Nayaka, R. Viswanatha, C.C. Vidyasagar, B.K. Chethana, Electrochemical synthesis and photocatalytic behavior of flower shaped ZnO microstructures, Powder Technology, 225 (2012) 232-238.
[55] M.M. Hassan, W. Khan, A. Azam, A.H. Naqvi, Effect of size reduction on structural and optical properties of ZnO matrix due to successive doping of Fe ions, Journal of Luminescence, 145 (2014) 160-166.
[56] A. Lagashetty, V. Havanoor, S. Basavaraja, S.D. Balaji, A. Venkataraman, Microwave-assisted route for synthesis of nanosized metal oxides, Science and Technology of Advanced Materials, 8 (2007) 484-493.
[57] G. Srinet, R. Kumar, V. Sajal, Effects of aluminium doping on structural and photoluminescence properties of ZnO nanoparticles, Ceramics International, 40 (2014) 4025-4031.
[58] E. Burstein, Anomalous Optical Absorption Limit in InSb, Physical Review, 93 (1954) 632-633.
[59] C. Bundesmann, M. Schubert, D. Spemann, T. Butz, M. Lorenz, E.M. Kaidashev, M. Grundmann, N. Ashkenov, H. Neumann, G. Wagner, Infrared dielectric functions and phonon modes of wurtzite $Mg_xZn_{1-x}O$(x 0.2), Applied Physics Letters, 81 (2002) 2376-2378.
[60] C.A. Arguello, D.L. Rousseau, S.P.S. Porto, First-Order Raman Effect in Wurtzite-Type Crystals, Physical Review, 181 (1969) 1351-1363.
[61] T.-L. Phan, Optical Properties of ZnO Nanoparticles Prepared by Mechanical Ball Milling, New Physics: Sae Mulli, 62 (2012) 483-487.
[62] M. Šćepanović, M. Grujić-Brojčin, K. Vojisavljević, S. Bernik, T. Srećković, Raman study of structural disorder in ZnO nanopowders, Journal of Raman Spectroscopy, 41 (2010) 914-921.
[63] O. Lupan, T. Pauporté, T. Le Bahers, I. Ciofini, B. Viana, High Aspect Ratio Ternary $Zn_{1-x}Cd_xO$ Nanowires by Electrodeposition for Light-Emitting Diode Applications, The Journal of Physical Chemistry C, 115 (2011) 14548-14558.
[64] O. Lupan, T. Pauporté, B. Viana, P. Aschehoug, M. Ahmadi, B.R. Cuenya, Y. Rudzevich, Y. Lin, L. Chow, Eu-doped ZnO nanowire arrays grown by electrodeposition, Applied Surface Science, 282 (2013) 782-788.
[65] O. Lupan, G.A. Emelchenko, V.V. Ursaki, G. Chai, A.N. Redkin, A.N. Gruzintsev, I.M. Tiginyanu, L. Chow, L.K. Ono, B. Roldan Cuenya, H. Heinrich, E.E. Yakimov, Synthesis and characterization of ZnO nanowires for nanosensor applications, Materials Research Bulletin, 45 (2010) 1026-1032.
[66] S.Y. Huang, Q.J. Cheng, S. Xu, D.Y. Wei, H.P. Zhou, J.D. Long, I. Levchenko, K. Ostrikov, Self-organized ZnO nanodot arrays: Effective control using SiNx interlayers and low-temperature plasmas, Journal of Applied Physics, 111 (2012) 036101.
[67] J. Liqiang, W. Dejun, W. Baiqi, L. Shudan, X. Baifu, F. Honggang, S. Jiazhong, Effects of noble metal modification on surface oxygen composition, charge separation and photocatalytic activity of ZnO nanoparticles, Journal of Molecular Catalysis A: Chemical, 244 (2006) 193-200.
[68] M. Bär, J. Reichardt, I. Sieber, A. Grimm, I. Kötschau, I. Lauermann, S. Sokoll, M.C. Lux-Steiner, C.-H. Fischer, T.P. Niesen, ZnO layers deposited by the ion layer gas reaction on $Cu(In,Ga)(S,Se)_2$ thin film solar cell absorbers: Morphology, growth mechanism, and composition, Journal of Applied Physics, 100 (2006) 023710.
[69] F. Säuberlich, J. Fritsche, R. Hunger, A. Klein, Properties of sputtered ZnO films and its interfaces with CdS, Thin Solid Films, 431–432 (2003) 378-381.
[70] J. Haber, J. Stoch, L. Ungier, X-ray photoelectron spectra of oxygen in oxides of Co, Ni, Fe and Zn, Journal of Electron Spectroscopy and Related Phenomena, 9 (1976) 459-467.

[71] Y. Tak, D. Park, K. Yong, Characterization of ZnO nanorod arrays fabricated on Si wafers using a low-temperature synthesis method, Journal of Vacuum Science & Technology B, 24 (2006) 2047-2052.
[72] Tables of Physical Quantities: A Handbook, Atomizdat, Moscow, 1976.
[73] A. Sundaresan, R. Bhargavi, N. Rangarajan, U. Siddesh, C.N.R. Rao, Ferromagnetism as a universal feature of nanoparticles of the otherwise nonmagnetic oxides, Physical Review B, 74 (2006) 161306.
[74] S. Banerjee, M. Mandal, N. Gayathri, M. Sardar, Enhancement of ferromagnetism upon thermal annealing in pure ZnO, Appl. Phys. Lett., 91 (2007) 182 501.
[75] M. Kapilashrami, J. Xu, V. Ström, K.V. Rao, L. Belova, Transition from ferromagnetism to diamagnetism in undoped ZnO thin films, Applied Physics Letters, 95 (2009) 033104.
[76] P.D. Sahare, V. Kumar, Optical and Magnetic Properties of Cu-Doped ZnO Nanoparticles, International Journal of Innovative Technology and Exploring Engineering, 3 (2013) 15-21.
[77] B. Panigrahy, M. Aslam, D.S. Misra, M. Ghosh, D. Bahadur, Defect-Related Emissions and Magnetization Properties of ZnO Nanorods, Advanced Functional Materials, 20 (2010) 1161-1165.
[78] G. Xing, D. Wang, J. Yi, L. Yang, M. Gao, M. He, J. Yang, J. Ding, T.C. Sum, T. Wu, Correlated d^0 ferromagnetism and photoluminescence in undoped nanowires, Applied Physics Letters, 96 (2010) 112511.
[79] Y. Zhang, E. Xie, Nature of room-temperature ferromagnetism from undoped ZnO nanoparticles, Applied Physics A, 99 (2010) 955-960.
[80] D.W. Abraham, M.M. Frank, S. Guha, Absence of magnetism in hafnium oxide films, Applied Physics Letters, 87 (2005) 252502.
[81] G.Z. Xing, Y.H. Lu, Y.F. Tian, J.B. Yi, C.C. Lim, Y.F. Li, G.P. Li, D.D. Wang, B. Yao, J. Ding, Y.P. Feng, T. Wu, Defect-induced magnetism in undoped wide band gap oxides: Zinc vacancies in ZnO as an example, AIP Advances, 1 (2011) 022152.
[82] B.B. Straumal, A.A. Mazilkin, S.G. Protasova, A.A. Myatiev, P.B. Straumal, G. Schütz, P.A. van Aken, E. Goering, B. Baretzky, Magnetization study of nanograined pure and Mn-doped ZnO films: Formation of a ferromagnetic grain-boundary foam, Physical Review B, 79 (2009) 205206.
[83] W.A. Adeagbo, G. Fischer, A. Ernst, W. Hergert, Magnetic effects of defect pair formation in ZnO, J. Phys.: Condens. Matter, 22 (2010) 436002.
[84] H. Peng, H.J. Xiang, S.-H. Wei, S.-S. Li, J.-B. Xia, J. Li, Origin and Enhancement of Hole-Induced Ferromagnetism in First-Row d^0 Semiconductors, Physical Review Letters, 102 (2009) 017201.

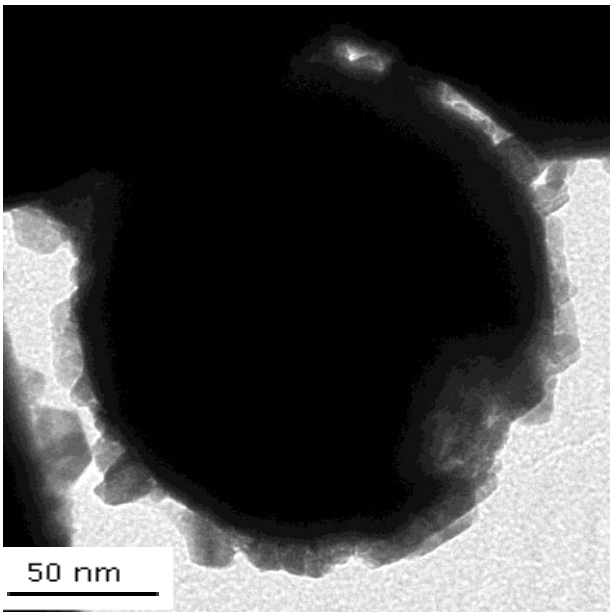

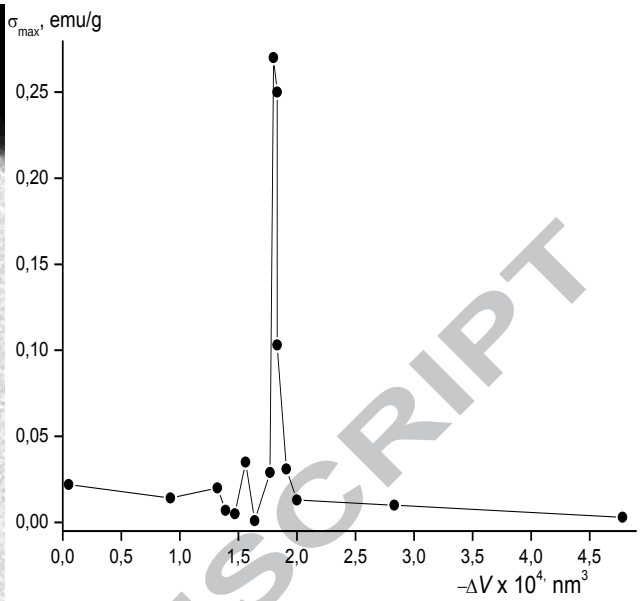

Highlights

- Levitation-jet aerosol synthesis of Zn particles capped by ZnO nanoparticles (NPs)
- TEM, XRD, UV-vis, FT-IR, Raman, XPS and magnetic characterization of the NPs
- Correlation between unit-cell volume of crystal lattice and maximum magnetization